Preprints.org

Article

Not peer-reviewed version

Epitaxial Growth of *p*-type β-Ga_2O_3 via Te and Mg Co-Doping Using Metal Organic Chemical Vapor Deposition

Chuang Zhang *, Hanzhao Song *, Chee Keong Tan *

Posted Date: 9 December 2025

doi: 10.20944/preprints202512.0642.v1

Keywords: β-Ga_2O_3; p-type doping; MOCVD growth; ultrawide bandgap semiconductor; valence band engineering

Preprints.org is a free multidisciplinary platform providing preprint service that is dedicated to making early versions of research outputs permanently available and citable. Preprints posted at Preprints.org appear in Web of Science, Crossref, Google Scholar, Scilit, Europe PMC.

Copyright: This open access article is published under a Creative Commons CC BY 4.0 license, which permit the free download, distribution, and reuse, provided that the author and preprint are cited in any reuse.

Preprints.org (www.preprints.org) | NOT PEER-REVIEWED | Posted: 9 December 2025
doi:10.20944/preprints202512.0642.v1

Disclaimer/Publisher's Note: The statements, opinions, and data contained in all publications are solely those of the individual author(s) and contributor(s) and not of MDPI and/or the editor(s). MDPI and/or the editor(s) disclaim responsibility for any injury to people or property resulting from any ideas, methods, instructions, or products referred to in the content.

Article

Epitaxial Growth of *p*-type *β*-Ga_2O_3 via Te and Mg Co-Doping Using Metal Organic Chemical Vapor Deposition

Chuang Zhang [1,*], Hanzhao Song [1,*,†] and Chee Keong Tan [1,2,3,*]

[1] Advanced Materials Thrust, Function Hub, Hong Kong University of Science and Technology (Guangzhou), Nansha, Guangzhou 511466, China
[2] Department of Electronic and Computer Engineering, Hong Kong University of Science and Technology, Hong Kong, China
[3] Guangzhou Municipal Key Laboratory of Materials Informatics, The Hong Kong University of Science and Technology (Guangzhou), Guangzhou, Guangdong 511453, China
* Correspondence: czhang885@connect.hkust-gz.edu.cn (C.Z.); hsong721@connect.hkust-gz.edu.cn (H.S.); cheekeongtan@hkust-gz.edu.cn (C.K.T.)
† This author contributed to the work equally with the first author.

Abstract

β-Gallium oxide (*β*-Ga_2O_3) offers considerable potential for next-generation power electronics due to its ultrawide bandgap (~4.9 eV) and established n-type conductivity. Nevertheless, realizing stable p-type doping remains a significant challenge, primarily due to the deep acceptor levels associated with conventional dopants. This article presents a co-doping strategy involving tellurium (Te) and magnesium (Mg), implemented via metal-organic chemical vapor deposition (MOCVD), aimed at addressing this challenge. Density-functional-theory (DFT) calculations suggest that Te incorporation could induce an intermediate band near the valence band maximum (VBM), potentially lowering the acceptor ionization barrier for Mg impurities. Initial experimental results indicate encouraging transport properties: the optimized Te-Mg co-doped thin film showed a room-temperature resistivity as low as 32.4 Ω·cm, with a measured Hall hole concentration of 1.78×10^{17} cm^{-3} and mobility of up to 5.29 $cm^2/V{\cdot}s$ at lower carrier concentrations (5.72×10^{14} cm^{-3}). Characterizations reveal evidence of VBM elevation via Te-Ga orbital hybridization and suggest a shift in the Fermi-level toward the valence band compatible with p-type behavior. While these preliminary findings show promise for enabling p-type Ga_2O_3 homoepitaxy, further research is necessary to optimize carrier concentrations below 1 Ω·cm, fully elucidate the Te-Mg doping dynamics, and provide more comprehensive device-level validation. This work introduces a pathway worthy of further exploration for achieving p-type conductivity in this critical semiconductor.

Keywords: β-Ga_2O_3; p-type doping; MOCVD growth; ultrawide bandgap semiconductor; valence band engineering

1. Introduction

β-Ga_2O_3 has emerged as a prominent candidate for next-generation semiconductor materials, particularly in power electronics applications. Its appeal arises from two key attributes: an ultrawide bandgap (~4.9 eV) and the relative ease of achieving n-type doping [1–5]. These characteristics distinguish *β*-Ga_2O_3 from other wide-bandgap semiconductors such as aluminum nitride (AlN) and diamond[6,7]. Recent advancements in melt-grown synthesis techniques have enabled the fabrication of bulk *β*-Ga_2O_3 crystals with diameters ranging from 6 to 8 inches [8–10], positioning this material as a cost-effective option for scalable production. Nonetheless, the absence of stable p-type conductivity remains a critical challenge for its full technological implementation [9,11]. This

© 2025 by the author(s). Distributed under a Creative Commons CC BY license.

Preprints.org (www.preprints.org) | NOT PEER-REVIEWED | Posted: 9 December 2025
doi:10.20944/preprints202512.0642.v1

limitation stems from difficult to introduce common acceptor elements with ionization energies of less than 1 Ev [12], which inherently restricts the formation of effective p-type conductivity.

To address the challenge of p-type conductivity in β-Ga_2O_3, researchers have explored heterojunctions with other p-type oxide semiconductors, such as nickel oxide (NiO) [1,13–15] and chromium trioxide (Cr_2O_3) [16,17], achieving significant advancements in device robustness and breakdown voltage. For instance, Ye, et al. [1] achieving significant advancements in device robustness and breakdown voltage. Several groups have further reported NiO/Ga_2O_3 rectifiers with high temperature blocking capabilities (8 kV) [14,18,19]. More recently, Su et al. [16] fabricated a p-Cr_2O_3/β-Ga_2O_3 heterojunction diode exhibiting a high ideality factor of 1.07 at 1.96 kV. Despite these advances, critical challenges persist in heterojunction integration, including lattice mismatch (for NiO/β-Ga_2O_3 is around 7.6% and for α-Ga2O3/β-Cr2O3 is around 5.9% [17,20]), crystallographic difference, and conduction band offset discrepancies [21]. These limitations hinder the realization of defect-free interfaces and optimal device performance.

Homoepitaxial p-type β-Ga_2O_3 is highly desirable for power and optoelectronic devices, yet conventional dopants such as Mg and Zn introduce deep traps (>1 eV) that pin the Fermi level and prevent hole activation [12,22], making the material resistive [23]. This difficulty is further driven by the oxygen 2p-dominated valence band, which limits hole transport [24]. To overcome this, Li et al. [25] fabricated Cu-doped p-type β-Ga_2O_3 through liquid-metal printing, Horng et al. [21,26] achieved p-type conductivity by phosphorus implantation enabling PN diodes, and our group[4] realized Se–Mg co-doping via ion implantation, where Se raises the valence band to reduce Mg activation energy[24,27]. However, these approaches lack potential for scalability. Therefore, epitaxial growth remains critical for achieving practical p-type β-Ga_2O_3 and enabling device integration.

This work presents a Te–Mg co-doping strategy to enable p-type conductivity in homoepitaxial β-Ga_2O_3 grown by metal–organic chemical vapor deposition (MOCVD). Hall measurements reveal a room-temperature resistivity as low as 32.4 Ω·cm with a corresponding hole concentration of 1.78×10^{17} cm^{-3}, while the highest hole mobility of 5.29 cm^2 V^{-1} s^{-1} is achieved at a carrier concentration of 5.72×10^{14} cm^{-3}. A positive Seebeck coefficient further confirms p-type conduction.

2. Materials and Methods

In this article, Te-Mg co-doped β-Ga_2O_3 films were deposited on semi-insulating Fe-doped β-Ga_2O_3 (010) substrates by MOCVD technique. The basic growth condition adopts a growth temperature of 500-700 °C and a growth pressure of 50 mbar. Triethylgallium (TEGa), diehtyltellurium (DETe) and oxygen were used as gallium (Ga), tellurium (Te) and oxygen (O) source respectively, which were kept constant at 500 standard center cubic per minute (sccm), 300 sccm and 2000 sccm. For samples denoted as T1, T2 and T3, the introduction of Mg source (Bis-cyclopentadienyl magnesium, Cp2Mg) varied from 0 to 10 sccm to 100 sccm.

The Hall measurement were measured using Toho HL-9900 and Physical Property Measurement System (PPMS, Quantum Design). The bandgap was investigated using UV-Vis spectroscopy (UV-Vis) and the Fermi level was measured using X-ray photoluminescence spectroscopy (VB-XPS).

First-principles calculations were performed using the Vienna Ab Initio Simulation Package (VASP) [17] with the projector-augmented wave (PAW) method [28,29]. A plane-wave basis set (cutoff energy = 520 eV) and Perdew-Burke-Ernzerhof generalized gradient approximation (GGA-PBE) functional [30] were employed for structural optimization, with convergence criteria set to 0.01 eV/Å (force) and 1×10^{-5} eV (self-consistent field energy). Calculated lattice constants (a = 12.46 Å, b = 3.09 Å, c = 5.88 Å, β = 103.69°) agreed well with experimental values. Electronic properties were derived using HSE06 hybrid functional (Hartree-Fock mixing parameter α = 0.39) [31]. Formation energies for impurities in charge states q were calculated using methods from ref[33]. Doping simulations employed an 80-atom β- Ga_2O_3 supercell (a 1×2×2 expansion of the conventional 20-atom unit cell, Figure 4a).

© 2025 by the author(s). Distributed under a Creative Commons CC BY license.

 doi:10.20944/preprints202512.0642.v1

3. Results and Discussion

Prior to homoepitaxial growth on β-Ga_2O_3 substrates, two heteroepitaxial samples (S1 and S2) were grown on (0001) sapphire substrates using metal-organic chemical vapor deposition (MOCVD) with Te-only (S1) and Te-Mg co-doping (S2). These samples were grown with triethylgallium (TEGa) and O_2 as the Ga and oxygen sources, respectively. Diethyltellurium (DETe) served as the Te source while bis(cyclopentadienyl)magnesium (Cp_2Mg) was introduced as the Mg source in S2. S1 utilized only DETe, establishing a baseline for Te-only doping. All the films were deposited with thickness controlled at 300 nm.

As summarized in Table 1, S2 exhibited significantly lower resistivity compared to S1, underscoring the role of Mg co-doping in enhancing electrical conductivity. Hall effect measurements in a van der Pauw configuration (Toho HL-9900) using direct current (DC) mode and magnetic field of ±1.5 T, performed using 20 nm/60 nm Ni/Au contacts, confirmed these trends (Figure 1a). Prior to Hall measurements, current-voltage (I-V) profiling verified Ohmic behavior of the contacts, as demonstrated in supplementary materials Figure S1.

Building on these results, three Te-Mg co-doped β-Ga_2O_3 thin films (T1–T3) were grown on insulating Fe-doped β-Ga_2O_3 (010) substrates under near-identical MOCVD conditions, with 300 nm thickness. Growth parameters are kept in confidentiality attributed to commercial purpose. Partial growth conditions and room-temperature (RT) Hall results for T1–T3 are detailed in Table 1.

Table 1. Partial growth condition and results of room temperature Hall measurement.

Sample	DETe	Cp_2Mg	Resistivity (Ohm·cm)	Hall mobility ($cm^2/V·s$)	Hall carrier concentration(cm^{-3})
S1	High	w/o	5865	0.19	$5.33×10^{15}$
S2	High	w/	94.3	0.457	$1.45×10^{17}$
T1	Low	w/	2064	5.29	$5.72×10^{14}$
T2	Medium	w/	908	1.51	$4.55×10^{15}$
T3	High	w/	32.4	1.08	$1.78×10^{17}$

To confirm the validity of the results, we conducted temperature-dependent Seebeck measurement for sample S2 and Hall measurement with varied magnetic field for sample T3, as shown in Figure 1 and Figure 2.

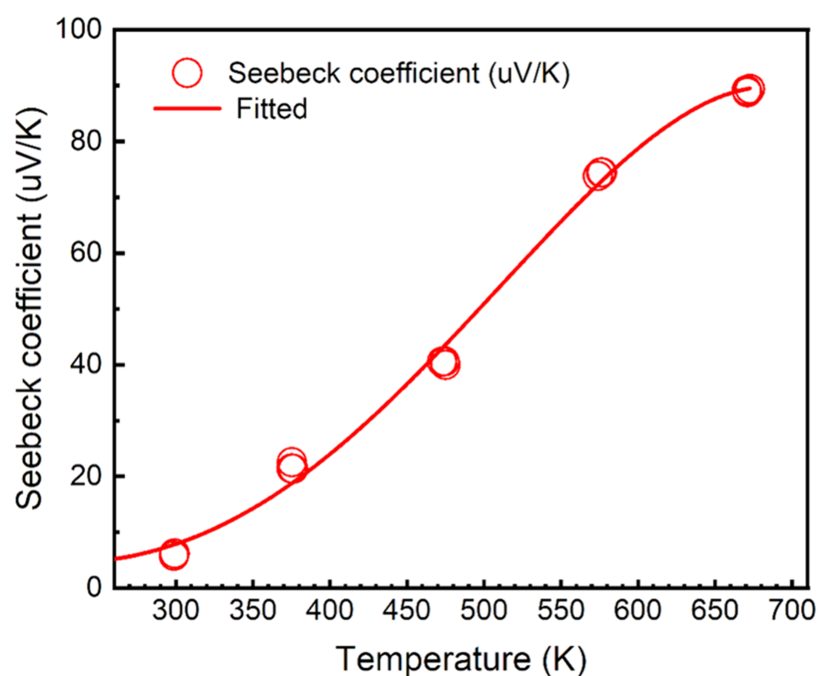

© 2025 by the author(s). Distributed under a Creative Commons CC BY license.

Preprints.org (www.preprints.org) | NOT PEER-REVIEWED | Posted: 9 December 2025
doi:10.20944/preprints202512.0642.v1

Figure 1. Temperature-dependent Seebeck coefficient for sample S2.

The temperature-dependent Seebeck measurement was conducted from room temperature to 674.15K (400°C) using a Thermoelectric Material Testing System (Cryoall CTA-3). The temperature gradient (ΔT) was set constant at 3K. As the results in Figure 1, where the Seebeck coefficient (S) is determined by $S = \Delta V/\Delta T$, S remains positive and increases with the overall temperature, indicating that S2 was a p-type semiconductor.

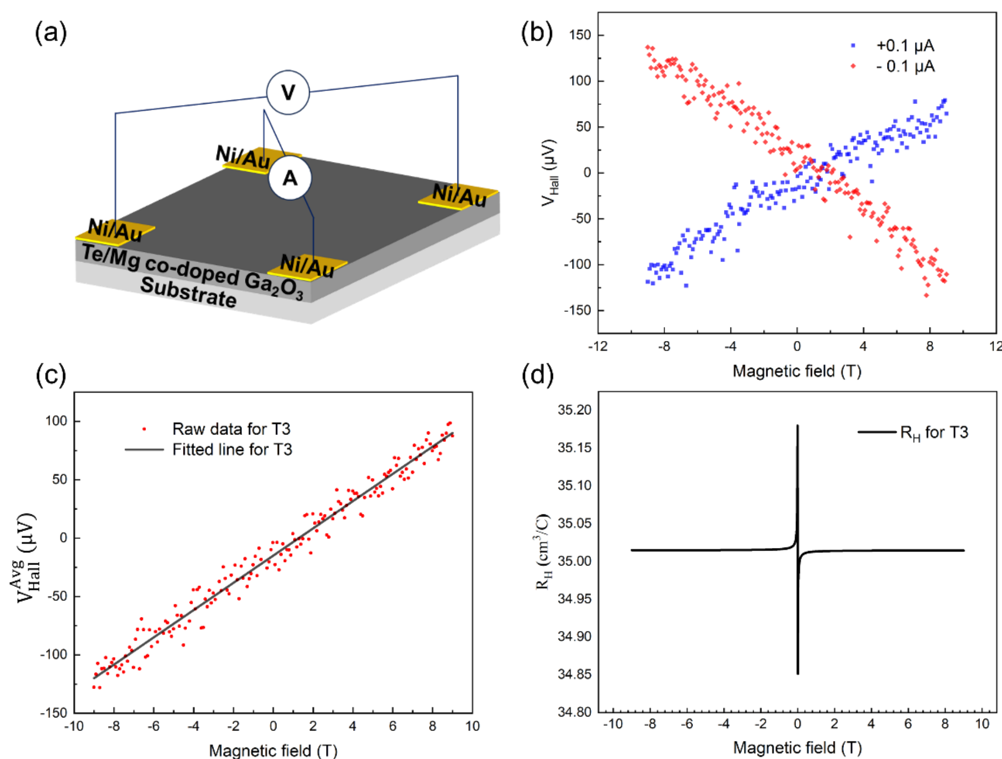

Figure 2. (a) Schematic demonstration of Hall measurement at van der Pauw configuration. (b) Hall voltage measured with magnetic field varying from -9 T to 9 T, (c) the averaged Hall voltage and (d) the calculated Hall coefficient for sample T3.

For sample T3, Hall measurement was conducted with magnetic field varied from -9 T to 9 T with an interval of 0.02 T, as shown in Figure 1(b)-1(d). The measurement was conducted using a Physical Property Measurement System (PPMS, Quantum Design) connected with external source meters (Keithley 6221 as DC source and Keithley 2182a as voltage monitor). Figure 1(b) shows the Hall voltage (V_{Hall}) under positive (+0.1μA, V_{Hall}^{+I}) and negative bias (-0.1μA, V_{Hall}^{-I}) with varying magnetic fields. To eliminate thermoelectric voltage and misalignment, the V_{Hall} in Figure 1(c) is acquired by averaging the results from Figure 1(b) ($V_{Hall}^{Avg} = \frac{V_{Hall}^{+I} - V_{Hall}^{-I}}{2}$). As depicted in Figure 1(c), the Hall voltage exhibited positive values under positive magnetic fields and negative values under negative magnetic fields, indicative of p-type conduction behavior. Figure 1(c) reveals nearly identical Hall coefficients of approximately 35.02 cm^3/C. The Hall mobility and carrier concentration are deduced to be 1.08 $cm^2/V\cdot s$ and 1.78×10^{17} cm^{-3} respectively, consistent with the prior findings presented in Table 1.

© 2025 by the author(s). Distributed under a Creative Commons CC BY license.

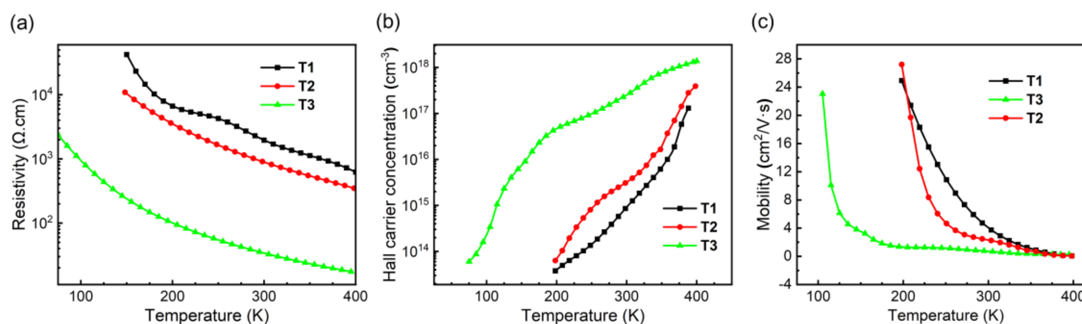

Figure 3. Temperature-dependent measurement for resistivity (a), Hall concentration (b) and mobility (c), for sample T1, T2 and T3.

Temperature-dependent Hall measurements were performed on homoepitaxial samples T1, T2, and T3 to evaluate their electrical properties, with van der Pauw configuration (Toho HL-9900) using DC mode and magnetic field of ±1.5 T, as shown in Figure 2. During measurement, Ohmic contacts were confirmed via IV profiling at 200 K for T1 and T2, and at 75 K for T3. As shown in Figures 2(a)–2(c), increasing Te doping concentration correlates with a decrease in resistivity (ϱ) and Hall carrier concentration (n_H), alongside a reduction in hole mobility (μ_H). These trends align with typical semiconductor behavior: higher doping introduces more charge carriers (n_H), which reduces resistivity (ϱ), while enhanced ionized impurity scattering lowers mobility (μ_H). Notably, sample T3, with the highest Te doping, exhibits the lowest resistivity (32.4 Ohm·cm) and highest carrier concentration (1.78 × 1017 cm^{-3} at RT), albeit with significantly reduced mobility (1.08 $cm^2/V{\cdot}s$). In contrast, sample T1, with the lowest Te content, achieves a high hole mobility of 5.29 $cm^2/V{\cdot}s$ at RT and 24.93 $cm^2/V{\cdot}s$ at 200 K, suggesting reduced scattering at cryogenic temperatures. The abrupt resistivity drops, and carrier concentration shift observed between T1 and T3 may stem from an optimal Te concentration required to balance dopant activation and defect states. Furthermore, the co-doping scheme likely introduces phonon dispersion effects, as evidenced by the pronounced mobility degradation at elevated temperatures.

Temperature-dependent Hall measurements reveal substantial scattering effects, consistent with expectations for co-doped materials. The observed rapid mobility declines and plateau-like drops in resistivity, for temperature from low to high, are attributable to extensive scattering. In supplementary calculations, we determined an effective mass of 0.34m0 but femtosecond-scale scattering times—indicating strong scattering behavior.

To further undercover the change on band structure, first-principles calculations were performed using the Vienna Ab Initio Simulation Package (VASP) [28] with the projector-augmented wave (PAW) method [29,30]. A plane-wave basis set (cutoff energy = 520 eV) and Perdew-Burke-Ernzerhof generalized gradient approximation (GGA-PBE) functional [31] were employed for structural optimization, with convergence criteria set to 0.01 eV/Å (force) and $1{\times}10^{-5}$ eV (self-consistent field energy). Calculated lattice constants (a = 12.46 Å, b = 3.09 Å, c = 5.88 Å, β = 103.69°) agreed well with experimental values. Electronic properties were derived using HSE06 hybrid functional (Hartree-Fock mixing parameter α = 0.39) [32]. Formation energies for impurities in charge states q were calculated using methods from ref[33]. Doping simulations employed an 80-atom β-Ga_2O_3 supercell (a 1×2×2 expansion of the conventional 20-atom unit cell, Figure 3a). In this supercell, Te doping replaced two Ga sites (%Te ~3.125%) or two O sites (%Te ~2.08%). Specifically, configurations involved substituting at two distinct Ga sites (GaI, GaII) and three distinct O sites (OI, OII, OIII), as detailed in Figure 2(b-f). The calculated total energies for these five configurations were -472.29068 eV, -472.92921 eV, -469.52646 eV, -468.05107 eV, and -468.71055 eV, respectively. Analysis revealed that the configuration with Te substituting at the OI site, which had the lowest total energy, is thermodynamically preferred.

© 2025 by the author(s). Distributed under a Creative Commons CC BY license.

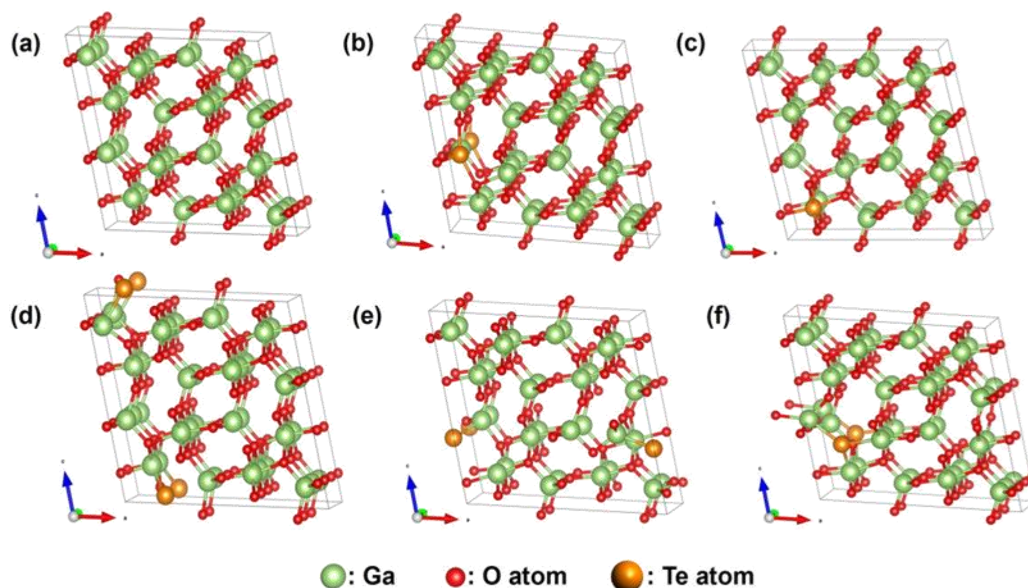

Figure 4. The model diagrams of β-Ga_2O_3 supercell, (a) undoped and Te doped at (b)Ga_I, (c)Ga_{II}, (d) O_I, (e)O_{II} and (f) O_{III} sites.

Formation energies in the neutral charge state were calculated for scenarios in which Te doping replaced three distinct oxygen sites (O_I, O_{II}, O_{III}) using methods from ref[33]. Under O-rich ($\mu_O = 0$) condition, formation energies for Te at OI, OII, and OIII sites were computed as -2.51 eV, -1.03 eV and -1.69 eV. Under O-poor ($\mu_{Ga} = 0$) conditions, they are 2.47 eV, 3.94 eV and 3.28 eV, respectively. We found that the formation energy is lower under O-rich conditions, suggesting that Te is suitable for replacing O atoms in β-Ga_2O_3 under these conditions. Notably, Te preferentially occupies O_I sites under both conditions due to the lowest formation energy ($O_I < O_{II} < O_{III}$).

Figure 4(a) shows the effective band structures of β-Ga_2O_3, it can be observed that the conduction band minimum (CBM) is positioned at the Γ-point, whereas the VBM is situated at the I-L line. The indirect energy bandgap of 4.8422 eV aligns well with the experimental values. As shown in Figure 4(b)-(d), the bandgap of β-Ga_2O_3 decreases when Te replaces different oxygen sites. Specifically, the bandgap is 2.475 eV when OI is replaced, 2.315 eV for O_{II}, and 1.989 eV for O_{III}. The VBM of Te-doped β-Ga_2O_3 is lifted because of atomic orbitals, similar effect has been reported for anion doping using Se [33,34].

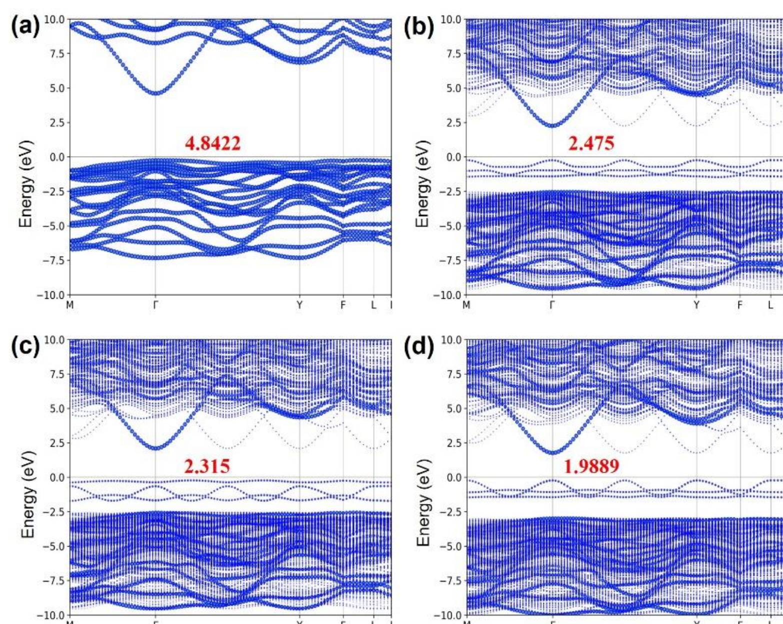

© 2025 by the author(s). Distributed under a Creative Commons CC BY license.

Figure 5. Calculated effective band structures of β-Ga_2O_3 (a) undoped and Te-doped at different oxygen sites: (b) O_I, (c) O_{II}, and (d) O_{III}.

To explain in more detail how the band structure changed, we analyzed the density of states of Te-doped β-Ga_2O_3. As depicted in Figure 5(a), the projected density of states (PDOS) illustrates that the band edges of pure β-Ga_2O_3 are dominated by O 2p and Ga 4s orbitals. The bandgap of β-Ga_2O_3 is determined by the occupancy of VBM by O 2p orbital electrons and the CBM by Ga 4s orbital electrons. Figure 5(b)-(d) shows the projected density of states of Te-doped β-Ga2O3 at different oxygen sites. According to atomic orbital theory, the energy level of Te 5p is higher than that of O 2p, and the localization of the VBM composed of O 2p derived states is reduced, which is beneficial for improving hole mobility.

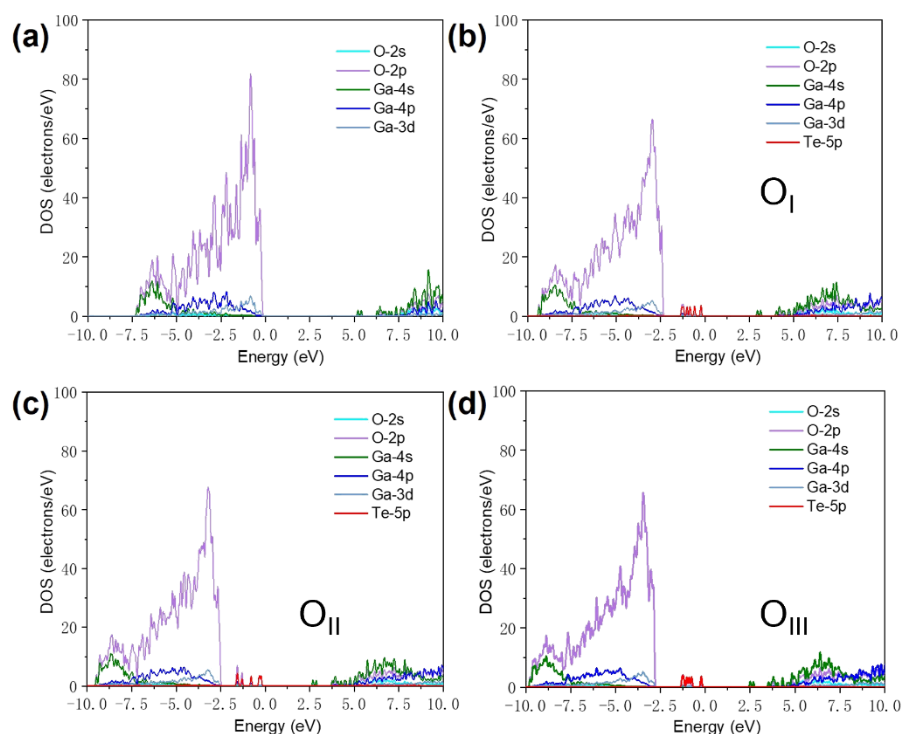

Figure 6. Density of states of (a) undoped and Te-doped β-Ga_2O_3 at different oxygen sites: (b) O_I, (c) O_{II}, and (d) O_{III}.

Figure 6(a) presents the VB-XPS results for Te-Mg co-doped β-Ga_2O_3 samples (T1–T3), calibrated against a silver reference. The VB edge energy decreases from 0.79 eV (T1) to 0.67 eV (T2) and 0.56 eV (T3) with increasing Te content, which reduced about 2.5 eV from the intrinsic sample (3.11 eV), confirming p-type carrier dominance as the Fermi level shifts toward the VBM. Complementary optical bandgap narrowing is observed in Figure 6(b), derived from Tauc plots using UV-Vis DRS. The bandgaps decreased from 4.42 eV (intrinsic) to 4.05 eV (T1), 3.46 eV (T2) and 3.34 eV (T3), paralleling the VB edge shift with Te doping. The optical bandgap measured in this study (4.05–3.34 eV, depending on Te content) is higher than simulated results for β-Ga_2O_3 with ~2% Te incorporation, suggesting that the actual Te content in samples T1–T3 is below 2%.

© 2025 by the author(s). Distributed under a Creative Commons CC BY license.

Preprints.org (www.preprints.org) | NOT PEER-REVIEWED | Posted: 9 December 2025 doi:10.20944/preprints202512.0642.v1

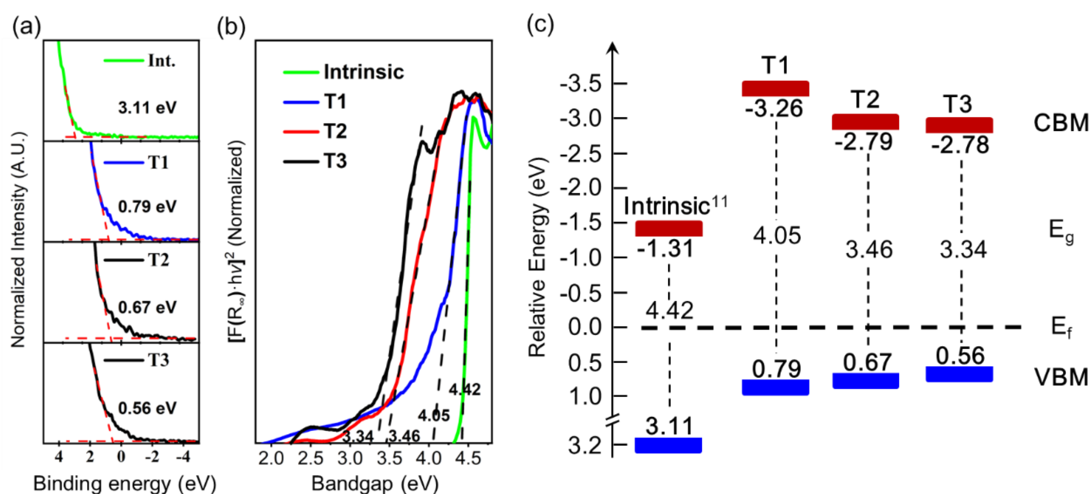

Figure 7. (a)VB-XPS (b) Tauc plot by UV-Vis diffuse reflectance spectroscopy (c) schematic description of band structure.

By combining data acquired from VB-XPS and UV-Vis DRS into the schematic band structure (Figure 7c), it reveals a systematic Fermi level migration in Te-Mg co-doped β-Ga_2O_3. Compared to intrinsic β-Ga_2O_3 [11] measured in another word from our group, where the Fermi level resides closer to the conduction band minimum (CBM), indicative of n-type conductivity, the co-doped samples exhibit a pronounced shift of the Fermi level toward the VBM. This transition confirms a fundamental change in carrier type, transitioning from donor-dominated (n-type) to acceptor-dominated (p-type) conductivity.

However, some refinements are still needed for further developing this co-doping technique. For instance, to increase carrier concentration and reduce the resistivity to below 1 Ohm·cm [35]. Besides, to better understanding the growth mechanism and carrier transport of the co-doping process is essential [36].

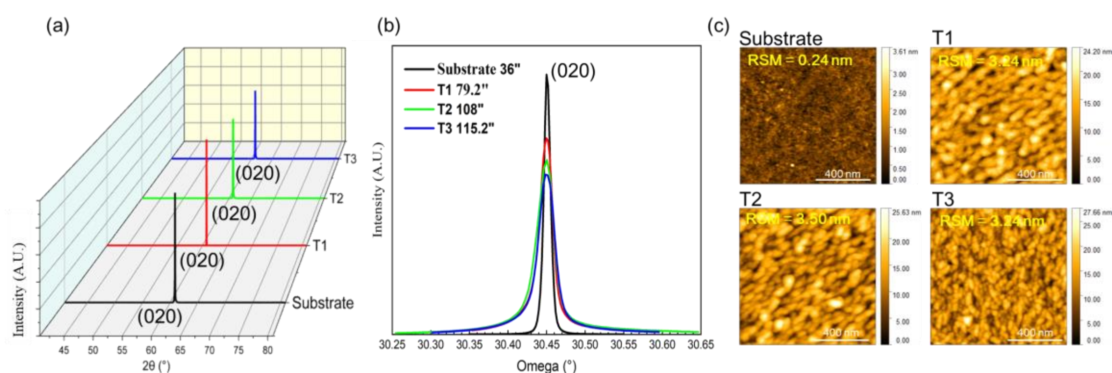

Figure 8. (a)XRD 2θ-ω scan. (b)XRD rocking curve. (c)Surface topography (1 nm × 1 nm) scanned by AFM for Fe-Ga_2O_3 substrate and sample T1 to T3.

Figure 8(a) and 8(b) reveal the crystalline quality of the synthesized films characterized by X-ray diffraction (XRD). Figure 8(a) shows that the p-type β-Ga_2O_3 film grows epitaxially along (020) direction of the substrate, exhibiting single-orientation growth that maintains the single-crystal structure. The crystalline quality was quantified using the full width at half maximum (FWHM) of the XRD rocking curve. Figure 8(b) shows the crystal quality of the film deteriorates from 79.2 arcsec to 115.2 arcsec, which indicated overall good crystal quality.

The change of structure and surface morphology before and after growth have been used for investigating using atomic force microscope (AFM), shown in Figure 7. The overall roughness of the

© 2025 by the author(s). Distributed under a Creative Commons CC BY license.

Preprints.org (www.preprints.org) | NOT PEER-REVIEWED | Posted: 9 December 2025 doi:10.20944/preprints202512.0642.v1

as-grown thin film is not small, potentially owing to the low growth temperature. As Te-doping increases, the grain size of the as-grown film becomes smaller, despite no obvious roughening, which demonstrates similar trends with what XRD rocking curves.

4. Conclusions

In summary, this article introduces a strategy for enabling p-type conductivity in β-Ga_2O_3 by employing Te-Mg co-doping via MOCVD, aiming to address a persistent challenge in this ultrawide-bandgap semiconductor. Initial findings suggest that the Te-Mg co-doping approach yields promising transport properties. Seebeck measurement confirms p-type semiconductor with positive Seebeck coefficient. Thin films fabricated with this strategy exhibited tunable hole conduction, with measured room-temperature carrier concentrations ranging from 5.72×10^{14} to 1.78×10^{17} cm^{-3} and corresponding resistivities between 2064 Ω·cm and 32.4 Ω·cm. A mobility value of 5.29 $cm^2/V\cdot s$ was measured under low-carrier-concentration conditions. Complementary DFT modelling provides a potential mechanism, indicating that Te incorporation appears to preferentially occupy oxygen sites, generating an intermediate band near the valence band. This mechanism is proposed to both lower the Mg acceptor ionization barrier and elevate the valence band maximum via orbital hybridization. Spectroscopy data (XPS, UV-Vis) show shifts consistent with the Fermi level moving towards the valence band and compatible with p-type behavior. While these initial results demonstrate the potential of the Te-Mg co-doping pathway, key challenges remain, such as substantially reducing the resistivity below 1 Ω·cm and improving doping efficiency. Future work will therefore focus on refining co-doping parameters, exploring post-growth treatments, and pursuing robust electrical validation. This study offers a potential pathway toward achieving p-type β-Ga_2O_3 worthy of deeper exploration.

Supplementary Materials: The following supporting information can be downloaded at the website of this paper posted on Preprints.org. The Current-voltage (I-V) curves before Hall measurements. Calculation for effective mass and scattering time.

Acknowledgments: The work is supported by C. K. Tan start-up fund from Hong Kong University of Science and Technology (Guangzhou), Guangzhou Municipal Science and Technology Project (No. 2023A03J0003, No. 2023A03J0013, No. 2023A04J0310 and No. 2023A03J0152), Department of Education of Guangdong Province (No. 2024ZDZX1005), Characterization and Preparation Facility (MCPF) and Green e Materials Laboratory at The Hong Kong University of Science and Technology (Guangzhou).

References

1. F. Zhou, H. Gong, M. Xiao, Y. Ma, Z. Wang, X. Yu, L. Li, L. Fu, H. H. Tan, Y. Yang, F.-F. Ren, S. Gu, Y. Zheng, H. Lu, R. Zhang, Y. Zhang, J. Ye, *Nature Communications* **2023**, 14.
2. Q. Zhang, N. Li, T. Zhang, D. Dong, Y. Yang, Y. Wang, Z. Dong, J. Shen, T. Zhou, Y. Liang, W. Tang, Z. Wu, Y. Zhang, J. Hao, *Nature Communications* **2023**, 14.
3. J. Zhang, P. Dong, K. Dang, Y. Zhang, Q. Yan, H. Xiang, J. Su, Z. Liu, M. Si, J. Gao, M. Kong, H. Zhou, Y. Hao, *Nat Commun* **2022**, 13, 3900.
4. Y. Wang, J. Cao, H. Song, C. Zhang, Z. Xie, Y. H. Wong, C. K. Tan, *Applied Physics Letters* **2023**, 123.
5. C. Zhang, S. Qi, J. Xue, J. Cao, Z. Xie, Y. Liao, Y. Wang, H. Song, A. Qu, G. Hu, Z. Mei, W. Tang, C. k. Tan, *Advanced Materials Technologies* **2024**, 10.
6. A. Qu, Z. Xie, Y. Wang, G. Hu, C.-K. Tan, *Journal of Electronic Materials* **2025**, 54, 3086.
7. J. Cao, Y. Wang, C. Zhang, G. Hu, W. Tang, G. Zeng, D. Gogova, C.-K. Tan, *Applied Physics Letters* **2025**, 126.
8. T. Igarashi, Y. Ueda, K. Koshi, R. Sakaguchi, S. Watanabe, S. Yamakoshi, A. Kuramata, *physica status solidi (b)* **2025**, 2400444.
9. S. Sun, C. Wang, S. Alghamdi, H. Zhou, Y. Hao, J. Zhang, *Advanced Electronic Materials* **2024**, 11.
10. X. Gao, K. Ma, Z. Jin, D. Wu, J. Wang, R. Yang, N. Xia, H. Zhang, D. Yang, *Journal of Alloys and Compounds* **2024**, 987.

© 2025 by the author(s). Distributed under a Creative Commons CC BY license.

Preprints.org (www.preprints.org) | NOT PEER-REVIEWED | Posted: 9 December 2025

doi:10.20944/preprints202512.0642.v1

11. Y. Liao, H. Song, Z. Xie, C. Zhang, C.-K. Tan, *Materials Today Advances* **2025**, 25.
12. A. Kyrtsos, M. Matsubara, E. Bellotti, *Applied Physics Letters* **2018**, 112.
13. Z. Zhang, Q. Song, D. Liu, Y. Yan, H. Chen, C. Mu, D. Chen, Q. Feng, J. Zhang, Y. Zhang, Y. Hao, C. Zhang, *Science China Materials* **2024**, 67, 1646.
14. W. Hao, Q. He, X. Zhou, X. Zhao, G. Xu, S. Long, in 2022 IEEE 34th International Symposium on Power Semiconductor Devices and ICs (ISPSD), 2022.
15. H. Gong, F. Zhou, W. Xu, X. Yu, Y. Xu, Y. Yang, F.-f. Ren, S. Gu, Y. Zheng, R. Zhang, H. Lu, J. Ye, *IEEE Transactions on Power Electronics* **2021**, 36, 12213.
16. C. Su, H. Zhou, Z. Hu, C. Wang, Y. Hao, J. Zhang, *Applied Physics Letters* **2025**, 126.
17. S. Ghosh, M. Baral, J. Bhattacharjee, R. Kamparath, S. D. Singh, T. Ganguli, *Journal of Applied Physics* **2021**, 130.
18. J.-S. Li, H.-H. Wan, C.-C. Chiang, X. Xia, T. Yoo, H. Kim, F. Ren, S. Pearton, *Crystals* **2023**, 13.
19. J.-S. Li, C.-C. Chiang, X. Xia, H.-H. Wan, F. Ren, S. J. Pearton, *Journal of Materials Chemistry C* **2023**, 11, 7750.
20. K. Kaneko, T. Nomura, S. Fujita, *physica status solidi c* **2010**, 7, 2467.
21. C.-Y. Huang, X.-Y. Tsai, F.-G. Tarntair, A. K. Singh, S.-H. Hsu, D.-S. Wuu, K. Järrendahl, C.-L. Hsiao, R.-H. Horng, *Materials Today Advances* **2025**, 25.
22. C. Zhang, X. Fu, H. Wang, *Materials Today Communications* **2024**, 40.
23. H. Peelaers, J. L. Lyons, J. B. Varley, C. G. Van de Walle, *APL Materials* **2019**, 7.
24. Y. Liao, H. Song, Z. Xie, C. Zhang, Z. Han, Y. Wang, C.-K. Tan, *Journal of Applied Physics* **2024**, 136.
25. Q. Li, B.-D. Du, J.-Y. Gao, J. Liu, *Applied Physics Reviews* **2023**, 10.
26. R. H. Horng, X.-Y. Tsai, F.-G. Tarntair, J.-M. Shieh, S.-H. Hsu, J. P. Singh, G.-C. Su, P.-L. Liu, *Materials Today Advances* **2023**, 20.
27. L. Luo, B. Zhou, Z. Liu, Q. Zhao, C. Wang, Z. Duan, Z. Xie, X. Yang, Y. Hu, *RSC Advances* **2023**, 13, 8476.
28. G. Kresse, J. Furthmuller, *PHYSICAL REVIEW B* **1996**, 54, 11 169.
29. G. Kresse, D. Joubert, *PHYSICAL REVIEW B* **1999**, 59, 1758.
30. P. E. Blochl, *Phys Rev B Condens Matter* **1994**, 50, 17953.
31. John P. Perdew, Kieron Burke, M. Ernzerhof, *PHYSICAL REVIEW LETTERS* **1996**, 77, 3865.
32. Jochen Heyd, Gustavo E. Scuseria, M. Ernzerhof, *JOURNAL OF CHEMICAL PHYSICS* **2003**, 118, 8207.
33. X. Liu, S. Ober, W. Tang, C.-K. Tan, *Journal of Materials Chemistry C* **2021**, 9, 7436.
34. H. Song, Z. Xie, Y. Liao, Y. Wang, C.-K. Tan, *Journal of Electronic Materials* **2024**.
35. Shuji Nakamura, G. Fasol, The Blue Laser Diode GaN Based Light Emitters and Lasers, Springer, **1997**.
36. Z. Chi, S.-R. Park, L. Burdiladze, T. Tchelidze, J.-M. Chauveau, Y. Dumont, S.-M. Koo, Z. Kushitashvili, A. Bibilashvili, G. Guillot, A. Pérez-Tomás, X.-Y. Tsai, F.-G. Tarntair, R. H. Horng, E. Chikoidze, *Materials Today Physics* **2024**, 49.

Disclaimer/Publisher's Note: The statements, opinions and data contained in all publications are solely those of the individual author(s) and contributor(s) and not of MDPI and/or the editor(s). MDPI and/or the editor(s) disclaim responsibility for any injury to people or property resulting from any ideas, methods, instructions or products referred to in the content.

© 2025 by the author(s). Distributed under a Creative Commons CC BY license.